

# Competing magnetic states, disorder, and the magnetic character of $\text{Fe}_3\text{Ga}_4$

J. H. Mendez,<sup>1</sup> C. E. Ekuma,<sup>1,2</sup> Y. Wu,<sup>1</sup> B. Fulfer,<sup>3</sup> J. C. Prestigiacomo,<sup>1</sup> W. A. Shelton,<sup>2,4</sup> M. Jarrell,<sup>1,2</sup>  
J. Moreno,<sup>1,2</sup> D. P. Young,<sup>1</sup> P. W. Adams,<sup>1</sup> A. B. Karki,<sup>1</sup> R. Jin,<sup>1</sup> Julia Y. Chan,<sup>5</sup> and J. F. DiTusa<sup>1,\*</sup>

<sup>1</sup>*Department of Physics & Astronomy, Louisiana State University, Baton Rouge, LA 70803, USA*

<sup>2</sup>*Center for Computation and Technology, Louisiana State University, Baton Rouge, LA 70803, USA*

<sup>3</sup>*Department of Chemistry, Louisiana State University, Baton Rouge, LA 70803, USA*

<sup>4</sup>*Department of Chemical Engineering, Louisiana State University, Baton Rouge, LA 70803, USA*

<sup>5</sup>*Department of Chemistry, University of Texas at Dallas, Richardson, TX 75080, USA*

(Dated: April 23, 2015)

The physical properties of metamagnetic  $\text{Fe}_3\text{Ga}_4$  single crystals are investigated to explore the sensitivity of the magnetic states to temperature, magnetic field, and sample history. The data reveal a moderate anisotropy in the magnetization and the metamagnetic critical field along with features in the specific heat at the magnetic transitions  $T_1 = 68$  K and  $T_2 = 360$  K. Both  $T_1$  and  $T_2$  are found to be sensitive to the annealing conditions of the crystals suggesting that disorder affects the competition between the ferromagnetic (FM) and antiferromagnetic (AFM) states. Resistivity measurements reveal metallic transport with a sharp anomaly associated with the transition at  $T_2$ . The Hall effect is dominated by the anomalous contribution which rivals that of magnetic semiconductors in magnitude ( $-5\mu\Omega$  cm at 2 T and 350 K) and undergoes a change of sign upon cooling into the low temperature FM state. The temperature and field dependence of the Hall effect indicate that the magnetism is likely to be highly itinerant in character and that a significant change in the electronic structure accompanies the magnetic transitions. We observe a contribution from the topological Hall effect in the AFM phase suggesting a non-coplanar contribution to the magnetism. Electronic structure calculations predict an AFM ground state with a wavevector parallel to the crystallographic  $c$ -axis preferred over the experimentally measured FM state by  $\approx 50$  meV per unit cell. However, supercell calculations with a small density of Fe-antisite defects introduced tend to stabilize the FM over the AFM state indicating that antisite defects may be the cause of the sensitivity to sample synthesis conditions.

PACS numbers: 75.30.Kz, 75.50.Bb, 75.50.Ee, 75.30.Cr

## INTRODUCTION

Metallic antiferromagnets have received renewed attention over the past few years, in part, because the iron pnictide and chalcogenide families of superconductors are derived via chemical substitutions into metallic antiferromagnetic parent compounds[1–3]. The character of the magnetic state in these materials, spin density wave (SDW) or more conventional local antiferromagnetism, has been explored and argued over as it has implications for the superconducting pairing mechanism[4]. Further fueling this interest is the discovery of the coexistence of itinerant ferromagnetism and local antiferromagnetism in the related material  $\text{Ba}_{1-x}\text{K}_x\text{Mn}_2\text{As}_2$ [5]. More recently and, perhaps more unexpectedly, the titanium-based pnictide oxide  $\text{Ba}_{1-x}\text{Na}_x\text{Ti}_2\text{Sb}_2\text{O}$  was discovered to have density wave states, spin (SDW) and/or charge, that coexist with a low temperature superconducting state[6]. This activity has built on a long history of exploration of antiferromagnets related to the cuprate superconductors as the interesting magnetic properties of these compounds are thought to be of central importance to their unconventional superconducting states[7]. The difficulty in separating out the important aspects of these complex materials has driven explorations of simpler antiferromagnetic metals such as elemental chromium[8], a

prototypical spin density wave material, and  $\text{GdSi}$ [9], a somewhat more complex system that has both itinerant and local magnetic moments participating in the magnetic ordering.

Here, we explore the properties of the lightly investigated Fe-based binary  $\text{Fe}_3\text{Ga}_4$ . This compound is both metallic and magnetic and there is a likely interdependence of local and itinerant magnetic moments that determine its magnetic state. In this material the close competition between antiferromagnetic (AFM) and ferromagnetic (FM) states is evidenced by several transitions between them as well as the sharp transition between the AFM phase and a field polarized paramagnetic (PM) phase that occurs with the application of magnetic field[10, 11]. Our data and simulations indicate that this competition between such obviously different magnetic states results from both its complex crystal structure, with its four unique crystallographic Fe sites each with a somewhat different magnetic moment and a large number of possible nearest-neighbor and next-nearest-neighbor interactions[12, 13], and the properties of the itinerant charge carriers. One indication of this coupling between the itinerant and more local moments is the temperature dependence of the metamagnetic field,  $H_{mm}$ , the field necessary to drive the transition from AFM to PM with a FM alignment of the field induced moments, which has the unusual feature

that it increases with temperature. Although the phenomenology of itinerant metamagnetism was worked out decades ago[14–16], in practice there are several different mechanisms that can cause abrupt transitions between AFM and field polarized PM states with field. For example, in  $(\text{Hf}_{1-x}\text{Ta}_x)\text{Fe}_2$  the symmetry of the crystal structure creates a magnetic frustration at one of the two crystallographically distinct Fe-sites. The magnetic moment at this site can be controlled via doping[17], and a larger magnetic moment at higher doping favors ferromagnetism. In  $\text{CoMnSi}$ , the field polarized PM-to-AFM instability appears to be closely related to the Mn-Mn separation within the orthorhombic crystal structure so that thermal expansion or chemical substitution causes an abrupt phase change[18, 19]. These materials are of interest for possible technological relevance as well since the closely competing magnetic orderings could allow applications as magneto-caloric elements[17–23].

The magnetic properties of  $\text{Fe}_3\text{Ga}_4$  have been previously characterized by susceptibility,  $\chi$ , and magnetization,  $M$ , measurements on polycrystalline samples which revealed several magnetic transitions[10, 24–27] between FM, AFM, and field polarized PM states. The ground state is FM with a transition to an AFM-like state near  $T_1 = 68$  K. This is accompanied by an unusual metamagnetism whereby  $H_{mm}$  increases dramatically with  $T$  up to  $T_2 \sim 360$  K[24]. The reduction of  $H_{mm}$  with cooling indicates a continuous decrease in the energy difference between the FM and AFM states until a first-order transition at  $T_1$  where the FM state emerges as the ground state. Above 400 K  $\chi$  is reduced[24] and the Mössbauer spectra evolves into a single broad line[28] so that a critical temperature for magnetic ordering was identified at 392 K. Mössbauer experiments have also established a different magnetic moment for each of the four unique crystallographic Fe-sites[24, 28] increasing the complexity of this binary system. Duijn *et al.* [26, 27] explored the specific heat and thermal expansion of  $\text{Fe}_3\text{Ga}_4$  finding only a small anomaly in the thermal expansion at  $T_1$ . The ability to grow polycrystalline grains of this material on GaAs substrates has led to the discovery of photomagnetic effects where an illumination enhanced magnetization was demonstrated[29]. This effect is most likely caused by simple heating through  $T_2$ , although the existence of a photon-mode photo-enhanced magnetization has been suggested[30]. Despite all of this interest, there have been almost no explorations of  $\text{Fe}_3\text{Ga}_4$  in single crystalline form[10, 11] and the identity of the magnetic states has not been established as neutron scattering experiments on powders were inconclusive[27].

We report on the magnetic, thermodynamic, and charge transport properties in single crystals of  $\text{Fe}_3\text{Ga}_4$  establishing a moderate anisotropy of the magnetic properties and the magnetic phase diagram for two orientations of an external magnetic field. We have carefully measured the specific heat of these crystals identifying

the magnetic contributions at  $T_1$  as well as the contribution above room temperature that grows near  $T_2$ . In addition, we have measured the resistivity,  $\rho$ , magnetoresistance (MR), and Hall effect of our crystals. The  $\rho$  is metallic and marked by an abrupt change at  $T_2$  while the MR displays sharp changes at  $H_{mm}$  both of which broadly reproduce the main findings of measurements on the polycrystalline samples[24, 27]. The  $T$  and  $H$  dependence of  $\rho$  hint at a close interdependence of the charge carriers and the ordered magnetic moments such as would occur in a SDW material. Our Hall measurements reveal a large anomalous Hall effect reaching  $-5 \mu\Omega\text{cm}$  in a 2 T field above room temperature, a value more representative of a magnetic semiconductor[31], and an ordinary Hall contribution consistent with a carrier concentration of 1 carrier per formula unit. Both the anomalous and ordinary terms show dramatic changes upon warming through  $T_1$  including a change of sign for the anomalous Hall effect from positive to negative, whilst the ordinary term remains positive. In addition, we observe a significant topological Hall effect,  $\rho_{THE}$ , indicating the possibility of a non-coplanar magnetic moment for finite fields at  $T_1 < T < T_2$ [32, 33].

To gain further insight into the causes of the competition between the magnetic phases and to help identify the magnetic order of the intermediate phase, between  $T_1$  and  $T_2$ , we have performed extensive electronic structure calculations. These calculations predict an AFM ground state with a wavevector along the crystallographic  $c$ -axis in contrast to the experimentally observed FM state. Furthermore, we show through supercell calculations performed with a small density of Fe atoms replacing Ga to mimic antisite disorder that the FM state can be stabilized. This suggests that disorder plays an important role in this material, and perhaps in other itinerant antiferromagnets, and can be used to effectively manipulate  $T_1$  in agreement with the observation of a sensitivity of this transition to synthesis conditions.

## EXPERIMENTAL DETAILS

Single crystals of  $\text{Fe}_3\text{Ga}_4$  were grown from high purity starting materials by standard iodine vapor transport techniques at 750 °C for 14 days[12, 13]. These crystals are black and shiny, and are roughly 1 mm by 1 mm by 2 mm thin brittle plates. All of the data presented in this paper were produced from crystals grown via iodine vapor transport methods. We have also employed optical furnace methods for synthesizing larger crystals and the main results of the structural and magnetic measurements were reproduced on these samples. Powder and single crystal X-ray diffraction, employing a Nonius Kappa CCD diffractometer ( $\text{Mo } K\alpha$ ,  $\lambda = 0.71073$  Å), were used to check the crystal structure and phase purity of our samples. No indication of any second phases

in the samples was detected and the X-ray results confirmed that the crystal structure is a base-centered monoclinic structure, space group  $C2/m$  as shown in Fig. 1. The cell volume,  $585.06(16) \text{ \AA}^3$ , and lattice parameters,  $a = 10.0979(15) \text{ \AA}$ ,  $b = 7.6670(15) \text{ \AA}$ , and  $c = 7.8733(10) \text{ \AA}$  with  $\beta = 106.298(7)^\circ$ , match previous measurements well. The single crystal X-ray measurements showed the  $c$ -axis to be aligned with the longest of the crystal dimensions and further details of these measurements are included in the Supplementary Materials. Crystals were annealed between 500 and 650 °C in an evacuated, sealed, fused silica tube and are compared to the results of a crystal that was sealed in a silica tube containing 1 atm of air and annealed at 550 °C to check for changes in the magnetic properties due to oxidation. No discernible differences were found between the crystals annealed in air and those annealed in vacuum.

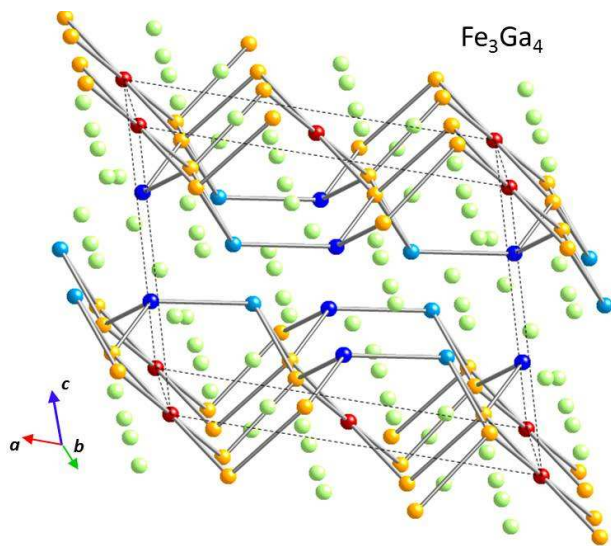


FIG. 1.  $\text{Fe}_3\text{Ga}_4$  crystal structure. The  $C2/m$  base-centered monoclinic structure demonstrating the four unique Fe positions in the unit cell with Fe1 shown in red, Fe2 in dark blue, Fe3 in light blue, and Fe4 in orange. Ga atoms are shown in green. There are four unique Ga sites in this crystal structure that are not differentiated in the figure. The shortest Fe-Fe bonds (less than the 2.96 Å between Fe2 sites) are highlighted.

A Quantum Design (QD) MPMSXL SQUID magnetometer equipped with a 5-T superconducting magnet was used to measure the magnetic susceptibility,  $\chi$ , and magnetization,  $M$ , of the crystals from 2 to 800 K. The  $M$  and  $\chi$  reported here have not been corrected for the effects of demagnetizing fields because of the difficulty associated with accurately determining demagnetization factors for oddly shaped single crystals. Comparisons with previous measurements performed on polycrystalline samples indicate that such corrections are not significant[24, 25]. Specific heat measurements were performed in a QD PPMS using a standard heat pulse technique from 2 to 400 K in zero field and with a slope-

analysis method in fields up to 0.5 T in the vicinity of  $T_1$ . The specific heat data were carefully corrected by subtracting the contribution from the measurement addenda. The electrical resistivity and Hall effect measurements were performed on rectangular-shaped samples polished with emery paper. Thin Pt wires were attached to four Epotek silver epoxy contacts with an average spacing between the voltage probes of 0.3 mm. The resistivity, magnetoresistance, and Hall effect measurements were performed at 19 Hz using standard lock-in techniques in a gas flow cryostat and a 5-T superconducting magnet. Hall effect measurements were corrected for any misalignment of the leads by symmetrizing the data collected at positive and negative fields.

## EXPERIMENTAL RESULTS

### Magnetic Properties of $\text{Fe}_3\text{Ga}_4$

The magnetic susceptibility of a  $\text{Fe}_3\text{Ga}_4$  single crystal is presented in Fig. 2 for two orientations of the magnetic field with respect to the crystallographic  $c$ -axis. There are several magnetic phases and phase transitions evident in our data including a sharp change in  $\chi$  at  $T_1 = 68 \text{ K}$ . Above  $T_1$  there is a wide temperature region of smaller  $\chi$  which evolves into a second region of large  $\chi$  above  $T_2 = 360 \text{ K}$ . At temperatures above  $T_3 = 420 \text{ K}$  the susceptibility is substantially reduced. We have indicated the hysteresis observed for increasing and decreasing temperatures in the regions surrounding  $T_1$  and  $T_2$  in the insets. A first order transition at  $T_1$  is indicated by the substantial hysteresis in this temperature range while hysteretic behavior is not clearly indicated at the higher temperature transitions. The phase transitions identified here match well those that were previously identified in polycrystalline samples[10, 24–27].

In addition to these more obvious features, we also observe a small decrease in  $\chi$  above  $T_4 = 685 \text{ K}$  that was noticed in very early investigations of the properties of  $\text{Fe}_3\text{Ga}_4$ [10] but ignored in subsequent treatments. This earlier work concluded that  $\text{Fe}_3\text{Ga}_4$  was magnetic below 697 K with a transition near 420 K to a second, higher moment, ferromagnetic phase[10]. At this point it is not apparent if this feature in  $\chi(T)$  is indicative of a subtle magnetic transition, a structural or electronic transition, or results from a small amount of a second phase. However, we have no evidence for a second phase within the samples from the X-ray diffraction investigations. We note that there are a few possible Fe, Ga, and O compounds that, if present, could provide a magnetic signal with a Curie temperature in this range. These include metastable  $\text{Fe}_{1-x}\text{Ga}_x$ , a dilution of bcc Fe with Ga, which has a Curie point near 685 K for  $x \sim 0.26$ [11]. In addition,  $\text{Fe}_{3-x}\text{Ga}_x\text{O}_4$  with  $x = 0.5$  is a possible impurity phase since its Curie temperature is also close to

$T_4$ [34, 35]. We point out, however, that multiple crystals grown under different conditions and annealing histories all displayed a similar signal, including those annealed in either vacuum or in air, and that the magnetic signal displays a substantial anisotropy below  $T_4$ . Thus, we consider it somewhat unlikely that  $\text{Fe}_{1-x}\text{Ga}_x$  or  $\text{Fe}_{3-x}\text{Ga}_x\text{O}_4$  impurities in the crystals would all contain the same Ga dilution level resulting in a magnetic transition at  $T_4$  in all samples measured over this temperature range. Attempts to fit a modified Curie-Weiss form to the data above 500 K were not satisfactory as the data are poorly represented by a simple paramagnetic response. This conclusion is consistent with earlier measurements on polycrystalline samples to higher temperatures where a Weiss temperature of 720 K and a fluctuating moment of  $J = 0.75$  (where the authors have assumed a  $g$ -factor of 2) were determined[25]. Further investigation of the structural and electronic properties of  $\text{Fe}_3\text{Ga}_4$  in proximity to  $T_4$  are necessary to resolve the cause of the change in the magnetic susceptibility we observe.

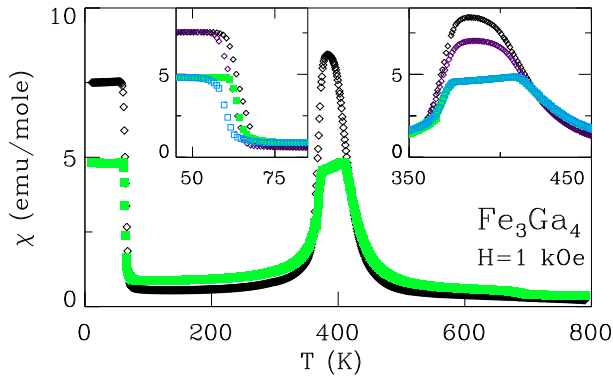


FIG. 2. Magnetic Susceptibility. Magnetic susceptibility of  $\text{Fe}_3\text{Ga}_4$  in a field of 1 kOe oriented parallel (black diamonds) and perpendicular (green squares) to the  $c$ -axis of the plate shaped crystals. Insets: Hysteresis observed upon cooling (purple diamonds and blue squares) and warming (black diamonds and green squares) in the temperature regions of the phase transitions. Note that in the temperature range between 350 and 450 K the warming and cooling scans result in nearly indistinguishable  $\chi$  for the case of the magnetic field perpendicular to the  $c$ -axis making the difference between the blue and green squares difficult to discern in right-most inset.

To better understand the nature of the different magnetic states identified in Fig. 2, we measured the isothermal magnetization at several temperatures between 4 and 400 K as displayed in Figs. 3 and 4. These data demonstrate both the similarities in  $M(H)$  for  $T < T_1$  and  $T > T_2$  K as well as the metamagnetic transition for intermediate  $T$ 's. The metamagnetic transition is observed to be particularly sharp for  $H$  parallel to the  $c$ -axis. Having single crystals has also allowed us to characterize the anisotropy in  $H_{mm}$ . As noticed in earlier investigations,

the critical field for this transition increases with  $T$ . We observe this unusual trend for both field orientations below 150 K. While  $H_{mm}$  continues to increase for fields parallel to the  $c$ -axis, the magnetization step size decreases with  $T$ . For fields perpendicular to the  $c$ -axis  $H_{mm}$  decreases for  $T$  above 150 K. We note that in this orientation, the data display two transitions indicating that the crystal was somewhat misaligned with the correct crystallographic orientation to observe only a single transition. The saturation magnetization,  $M_S$ , at low  $T$  corresponds to  $1.5 \mu_B$  per Fe somewhat larger than the magnetic moment estimated from Mössbauer measurements ( $1.38 \mu_B/\text{Fe}$ )[24] and that seen in the previous  $M_S$  measurements of polycrystalline samples ( $1.17$  to  $1.27 \mu_B/\text{Fe}$ )[25, 27].

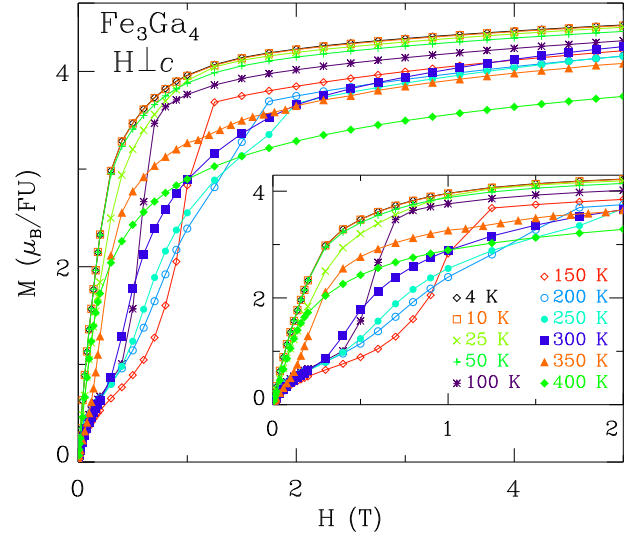


FIG. 3. Magnetization. Magnetization,  $M$ , of single-crystal  $\text{Fe}_3\text{Ga}_4$  measured with a field,  $H$ , oriented perpendicular to the  $c$ -axis of the crystal. Temperatures are indicated in the figure. Inset: Low field  $M(H)$  plotted to highlight the rapid changes to  $M$  below 2 T.

The magnetization, its anisotropy, and the hysteresis associated with the metamagnetic transition in a crystal grown at a later time via iodine vapor transport and treated in the same manner are demonstrated in Fig. 5. A hysteresis of about 400 Oe is evident when the crystal is oriented with its  $c$ -axis parallel to the magnetic field while a much smaller history dependence is observed when the crystal is rotated so that  $H$  is perpendicular to the  $c$ -axis. The similarity of the magnetic response at 2 K and 400 K is also displayed in the figure which motivates our identification of a FM phase below  $T_1$  and between  $T_2$  and  $T_3$ . However, we note that demagnetization effects may reduce the differences apparent in these curves and that the temperature dependence of  $\chi$  is not that of a prototypical PM-to-FM transition above 350 K. Thus, it remains a possibility that the magnetic state between  $T_2$  and  $T_3$  is more complex, such as a canted AFM state

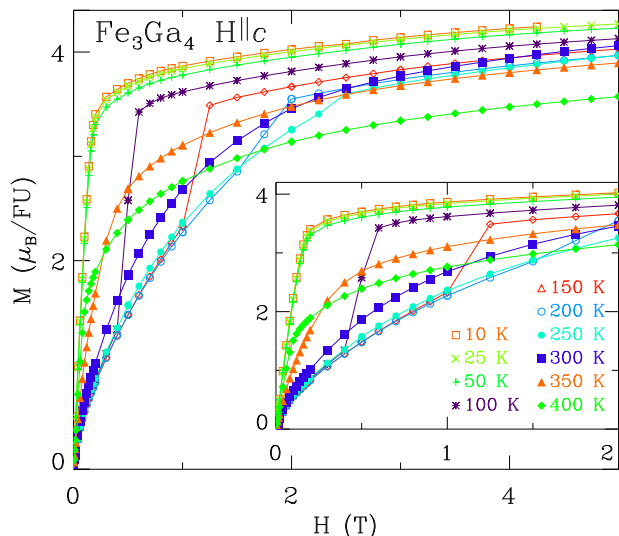


FIG. 4. Magnetization,  $M$ , parallel to the  $c$ -axis. Same sample as in 3. Temperatures are indicated in the figure. Inset: Low field  $M(H)$  plotted to highlight the rapid changes to  $M$  below 2 T.

with a FM component making neutron diffraction experiments essential to resolving the magnetic state in this  $T$  range.

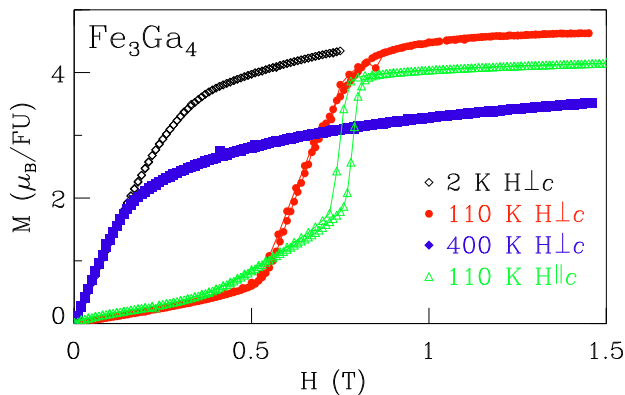


FIG. 5. Low Field Magnetization. Magnetization displayed in two different field orientations with respect the  $c$ -axis. Data shown at three temperatures to demonstrate the variations that occur in the three distinct magnetically ordered regions that we have identified.

The variation of the magnetic transition temperatures of the samples with annealing mentioned above suggests that the magnetic state is sensitive to subtle changes to the stoichiometry, disorder, or crystal structure of the samples. We observed that the as-grown samples can have substantially reduced values of  $T_1$ ,  $T_2$ , and  $T_3$ , but annealing at 550 °C was sufficient to increase these transition temperatures so that they more closely matched those found in the previously measured polycrystalline

samples [10, 24, 27].

### Specific Heat of $\text{Fe}_3\text{Ga}_4$

The specific heat,  $C_P$ , of a single crystal of  $\text{Fe}_3\text{Ga}_4$  is shown in Fig. 6 where  $C_P/T$  is displayed between 2 and 400 K. There are two features of these data that are likely of magnetic origin. The first is a small peak near  $T_1$  and the second is the shoulder seen above 350 K. To better understand the likely contributions to  $C_P(T)$  we have fit a simplified model of the phononic and electronic contributions to  $C_P(T)/T$  to the data that is represented in the figure by the solid line. This model contains a Debye and three separate Einstein modes to represent the complicated phonon density of states of  $\text{Fe}_3\text{Ga}_4$ . It also includes a linear temperature dependent term to model the electronic contributions which can dominate  $C_P$  at low  $T$ , although magnons terms may also contribute. We found that including a larger number of independent Einstein terms did not significantly increase the quality of the fit, so we report this minimal model to describe the data. The best fit value of the parameters included a Debye temperature  $\Theta_D = 120$  K, Einstein temperatures of  $\Theta_E = 135, 260$ , and  $365$  K, and a linear-in-temperature coefficient,  $\gamma$ , of  $21$  mJ/mole K<sup>2</sup>. We have also included in our modeling an estimated correction (dashed-dotted line) to account for the difference between  $C_P$  and the heat capacity taken at constant volume. This correction is based upon the thermal expansion and compressibility of  $\text{Fe}_3\text{Ga}_4$  as reported in Ref. [27]. The estimated additional contribution due to the thermal expansion of the sample can be seen above  $\sim 150$  K.

In Fig. 7 we display the same  $C_P(T)$  data at  $T < 20$  K using the standard form for exploring the low  $T$  specific heat of solids by plotting  $C_P(T)/T$  as a function of  $T^2$ . Here we plot the results of the fitting procedure described above represented by the solid line in the figure. We have also included a fit of a linear dependence between 2 and 10 K to represent the standard  $C_P/T = \gamma + \beta T^2$  form, dashed line. The best fit value for  $\gamma$  is  $23$  mJ/mole K<sup>2</sup> and the  $\beta$  value found corresponds to  $\Theta_D = 125$  K in reasonable agreement with the more complex model described above giving us confidence that our fitting procedure gives us a good impression of the lattice and conduction electron contributions to the specific heat.

The two features of the data that we suggested above are of magnetic origin are clearly not described by our models shown in Fig. 6. The first, the sharp peak at  $T_1$ , is highly sensitive to  $H$  as we demonstrate in the upper inset to Fig. 6. Here the application of magnetic field is seen to drive the transition to higher  $T$  and to decrease the size of the anomaly such that by 0.5 T we find no indication of a sharp anomaly in  $C_P(T)$  in this  $T$  range. These data were taken with a slope-analysis method which makes use of the measured change in the



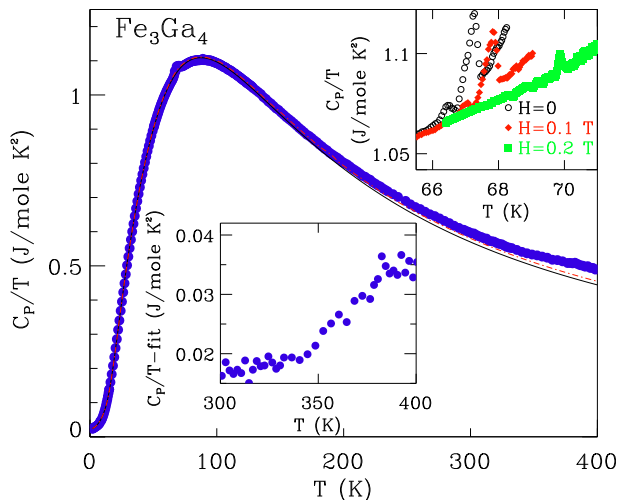


FIG. 6. Specific Heat. Specific heat,  $C_P$  divided by temperature,  $T$ , as function of  $T$ . Solid line represents a fit of a model of the phonon contribution to the specific heat, see text for details. Dashed-dotted line includes a correction to the model to better represent the heat capacity at constant pressure based upon the thermal expansion and compressibility[27]. Upper inset:  $C_P$  as measured by a slope analysis method between 66 and 71 K at magnetic fields,  $H$  identified in the figure. Lower inset: the difference between the measured  $C_P$  (at  $H = 0$ ) and the model for the phonon contribution, fit, between 300 and 400 K demonstrating a substantial increase for  $T > 350$  K.

$T$  of the sample platform over small intervals of  $T$  during a warming or cooling cycle to give greater sensitivity near sharp phase transitions. Our model of the phonon contributions also fails to properly fit the  $C_P(T)$  data above 150 K with the difference between data and model growing slowly until 350 K where a steep increase in this difference is apparent in the lower inset to Fig. 6. The onset of this contribution near 350 K corresponds well with  $T_2$  identified in  $\chi(T)$  and, thus, we identify this anomaly with this transition. The entropy,  $S$ , associated with the transition at  $T_1$  found using the relation  $\Delta S = \int C_P(T)/T dT$  is small,  $\sim 17$  mJ/mole K, or  $\sim 0.2$  % of  $R \ln(2J + 1)$ , where we have made use of the estimated average value for  $J = 0.75$  from  $M_S$  (Figs. 3 and 4). Thus, the transition from the low  $T$  FM state to the tentatively identified AFM state at  $T_1$  does not involve a large entropy change. We have also estimated  $\Delta S$  associated with the rise in  $C_P(T)$  above  $T_2$  finding  $\Delta S = 0.43$  J/mole K between  $T_2$  and 400 K providing an upper bound to the magnetic entropy change.

A tentative phase diagram based upon our  $M(H, T)$  and  $C_P(T)$  data is presented in Fig. 8 to demonstrate the overall behavior that we have observed. A phase diagram based on polycrystalline measurements can be found in Ref. [27]. Here, we have employed the earlier designations for the phases that were assigned as ferromagnetic and antiferromagnetic, but these are also only

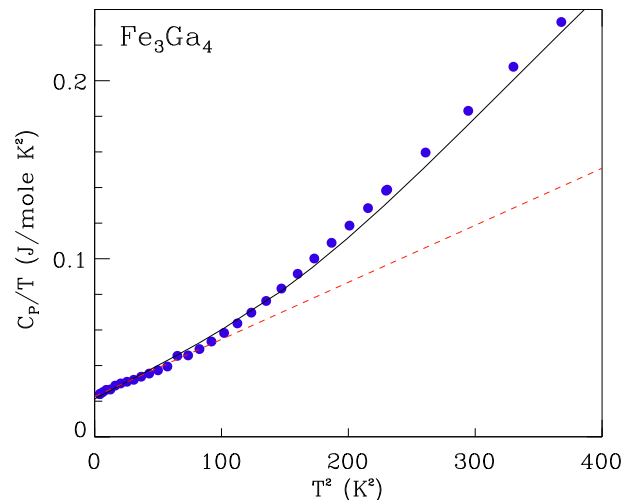


FIG. 7. Low Temperature Specific Heat. Specific heat,  $C_P$  divided by temperature,  $T$  as function  $T^2$  below 20 K. Solid line represents the same fit of a model of the phonon contribution to the specific heat as in Fig. 6 while the dashed line represents a fit of the simple model  $C_P(T)/T = \gamma T + \beta T^2$  to the data below 10 K.

tentative as neutron scattering experiments to date have been inconclusive[27]. The anisotropy in  $H_{mm}$  above 150 K is evident and defines a large portion of the phase diagram. The open symbols designate fields where we observe changes in  $dM/dH$  which may indicate a rearrangement of magnetic domains in the FM phase. In Fig. 8 we have also indicated  $T_4$  where we observe a small increase in  $\chi$ . The dashed line in the figure is merely a designation of the crossover between the FM and PM state at finite field that is poorly defined and that we have not adequately explored.

### Electrical Transport Properties of $\text{Fe}_3\text{Ga}_4$

The electrical resistivity,  $\rho$ , magnetoresistance, MR, and Hall effect of our crystals were measured in a configuration where the current was along the  $c$ -axis of the crystals and the field was perpendicular to the direction of the current (transverse MR).  $\rho(T)$  shown in Fig. 9 can be compared to previous measurements performed on polycrystalline samples[10, 26]. The behavior is metallic with a residual resistivity ratio (RRR) of 2.7 and a strong anomaly near  $T_2$  (close to 310 K for the crystal whose  $\rho$  is shown in the figure). Although the room- $T$  value for  $\rho$  ( $\sim 200 \mu\Omega \text{ cm}$ ) is smaller than in previous measurements, the RRR is significantly smaller than that found by Duijn[27]. No easily identifiable anomaly near  $T_1$  was observed. In agreement with Ref. [27] we find a low  $T$   $\rho$  that is well described by a  $T^2$  dependence consistent with the moderately enhanced  $\gamma$  observed in  $C_P(T)$ .

We find a negative MR,  $\Delta\rho/\rho_0$  where  $\Delta\rho = \rho - \rho_0$

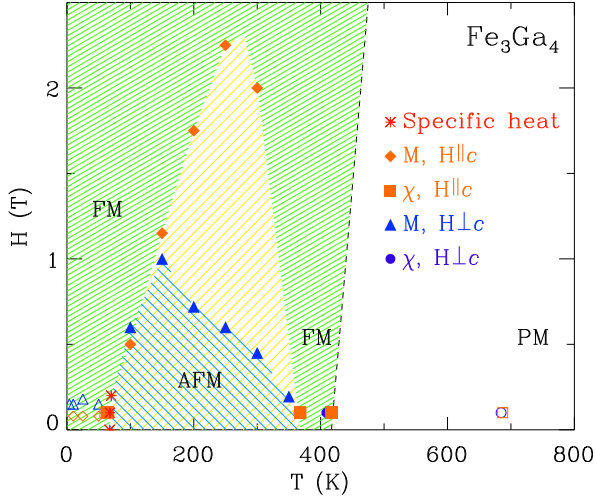


FIG. 8. Phase Diagram. Temperature,  $T$ , and magnetic field,  $H$ , phase diagram of  $\text{Fe}_3\text{Ga}_4$  based on magnetization,  $M$ , susceptibility,  $\chi$ , and specific heat measurements. Symbols represent the phase boundaries determined by the maxima of the  $H$ -derivatives of the isothermal  $M$ , maxima of the  $T$  derivatives of  $\chi$ , and maxima in  $T$  dependence of the specific heat. These phase boundaries are plotted for  $H$  in both the  $H \perp c$  and the  $H \parallel c$  configurations as indicated in the figure. Zero field magnetic phases are tentatively assigned as ferromagnetic, FM, antiferromagnetic, AFM, or PM, as indicated in the figure. Data at 685 K indicate  $T_4$  where a weak peak in  $d\chi/dT$  is observed which may indicate a phase transition, but that has not been fully characterized.

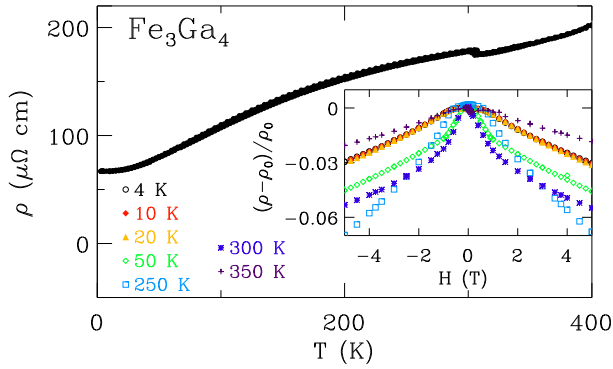


FIG. 9. Resistivity and Magnetoresistance. The zero-field resistivity,  $\rho$ , as a function of temperature,  $T$ . Inset: Magnetoresistance,  $(\rho(H) - \rho_0)/\rho_0$ , where  $H$  is the magnetic field and  $\rho_0$  is the zero-field resistivity, at temperatures indicated by the key in the main frame.

and  $\rho_0$  is the zero-field value of  $\rho$ , at all temperatures investigated (between 4 and 350 K) as displayed in the inset to Fig. 9. This is in contrast to the previously published work on polycrystalline materials[27] where a positive MR was found below 15 K and where a positive contribution was apparent above 350 K. A negative MR is to be expected for itinerant ferromagnets where

the field dependence of the carrier fluctuation scattering can dominate, particularly near phase transitions[36]. The low-field negative MR appears to be at a maximum near  $T_2$  where the anomaly in the  $\rho(T)$  is observed. In addition, we also find discontinuous changes to  $d\rho/dH$  at fields close to saturation. The  $\Delta\rho/\rho_0$  values at 5 T are nearly a factor of 2 smaller than that reported by Duijn[27] most likely due to the larger residual resistivity of our crystals.

In magnetic materials the Hall effect is usually dominated by the anomalous contributions, referred to as the anomalous Hall effect (AHE), stemming from spin-orbit coupling (intrinsic) or spin orbit scattering (extrinsic) contributions[31, 33]. This expectation is met in  $\text{Fe}_3\text{Ga}_4$  as we demonstrate in Fig. 10 where a Hall resistivity,  $\rho_{xy}$ , as large as  $-5 \mu\Omega \text{ cm}$  at 5 T is observed. The field dependence of  $\rho_{xy}$  resembles that of  $M(H)$  from the same crystal in the same orientation presented in Fig. 3. Besides the large magnitude of  $\rho_{xy}$  at high temperatures, the most apparent feature is its change of sign at  $\sim 100$  K.

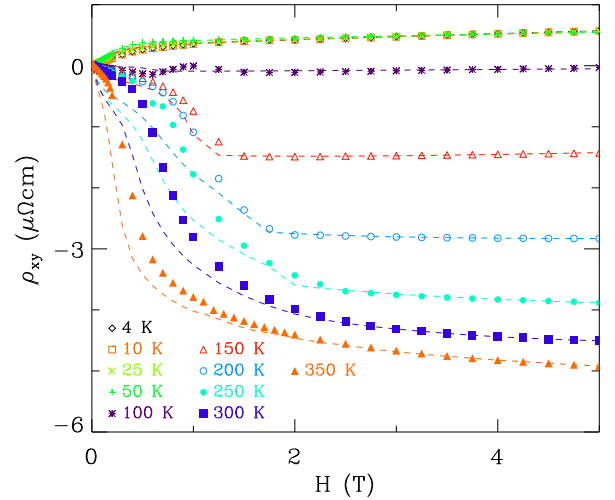


FIG. 10. Hall effect. The Hall resistivity,  $\rho_{xy}$  of  $\text{Fe}_3\text{Ga}_4$  vs. magnetic field,  $H$ , at temperatures indicated in the figure. Dashed lines are fits of a standard model of the anomalous Hall effect, see text for details.

In order to quantify the Hall constants and better understand the relationships between the ordinary and anomalous contributions to  $\rho_{xy}$ , we fit the usual model for the AHE, which is described by the expression  $\rho_{xy} = R_0 H + 4\pi M R_S$ , to the data. In this model  $R_0$  is the ordinary Hall constant which is closely related to the sign and density of the conducting carriers and  $R_S$  is the anomalous Hall constant.  $R_S$  has been shown to be proportional to  $\rho^2$  when the intrinsic or side-jump scattering mechanisms dominate, and to  $\rho$  when the skew-scattering mechanism is largest (at very low resistivities). Since the intrinsic mechanism is thought to describe materials in the resistivity range of our  $\text{Fe}_3\text{Ga}_4$  crystals (Fig. 9), we

have assumed a  $R_S = S_H * \rho^2$  dependence when interpreting the anomalous term. The dashed lines shown in Fig. 10 are the results of this fitting procedure,  $\rho_{xy-fit}$ , where the high field data were more heavily weighted since the magnetization is near saturation and the linear dependence of  $\rho_{xy}/H$  on  $M/H$  is more apparent. While this model describes the data qualitatively well, there are distinct differences between the data and model at low fields. To highlight these differences, we plot the residual Hall effect, the difference between the data and the model,  $\rho_{THE} = \rho_{xy} - \rho_{xy-fit}$ , in Fig. 11. It is interesting to note that  $\rho_{THE}$  is largest in the field region where  $dM/dH$  is largest, that is in the range 0.1 to 1 T. It is clear from a comparison of the low field  $\rho_{xy}$  in Fig. 10 and  $M(H)$  in Fig. 3 that the magnetization has a low field contribution that is missing from the AHE. There are two possible reasons for the failure of the model to capture this low field behavior. The first is to speculate that the low field  $M(H)$  is dominated by an extrinsic contribution most likely a magnetic second phase that charge carriers are not sensitive to. However, this would require a large portion of the crystals,  $\sim 10\%$ , to be made up of this second phase, which is not consistent with the X-ray diffraction data. Instead, we assert that there is likely a non-coplanar magnetic moment at low fields in  $\text{Fe}_3\text{Ga}_4$  so that an AHE stemming from a topological contribution to the Hall effect,  $\rho_{THE}$ , is responsible for the difference between the data and the simple model[32, 33, 37–39]. Since there are no reliable data determining the character of the magnetic order in  $\text{Fe}_3\text{Ga}_4$  we are not able to completely resolve this issue at this time.

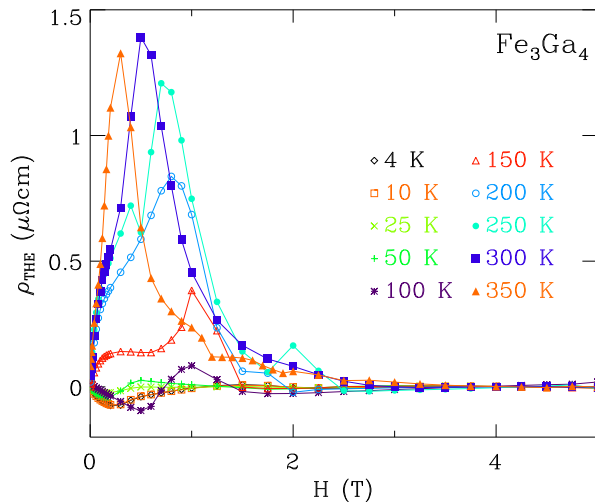


FIG. 11. Topological Hall Effect. The topological contribution to the Hall resistivity of  $\text{Fe}_3\text{Ga}_4$   $\rho_{THE} = \rho_{xy} - \rho_{xy-fit}$  - where  $\rho_{xy-fit}$  corresponds to the dashed lines in Fig. 10, vs. magnetic field,  $H$ , at temperatures indicated in the figure.

The Hall parameters determined from our fitting procedure,  $R_0$  and  $R_S$ , are presented in Fig. 12. There are several features of these data that are striking. While the

ordinary Hall constant is positive, hole-like carriers, below room temperature with a value consistent with a single carrier per  $\text{Fe}_3\text{Ga}_4$  formula unit,  $R_S$  is large ( $\sim -0.1 \text{ cm}^3/\text{C}$  near room temperature and  $\sim 0.01 \text{ cm}^3/\text{C}$  at low temperature) and undergoes a sign change near 100 K. The change in  $R_S$  from positive at low  $T$  to negative above 100 K reflects the change of sign of  $\rho_{xy}$  at this  $T$  and appears to correlate well with a strong increase of  $R_0$  between 100 and 150 K as well as the change in the magnetic state of the system in this temperature and field range (see Fig. 8). The decoupling of  $R_0$  and  $R_S$  is highlighted by this feature of the data and further supports our assumption that the AHE results from intrinsic,  $k$ -space Berry's phase related, effects. This feature may also indicate interesting variations to the spin-orbit coupling as the Fermi surface evolves due to the changing magnetic state. As a point of comparison, we estimate the parameter  $S_H = R_S/\rho^2$  to be  $2.4 \times 10^4 \text{ Am/V}^2\text{s}$  which is smaller than found in MnSi and MnGe, but comparable to values found in other Fe-containing itinerant magnets FeGe and  $\text{Fe}_{1-x}\text{Co}_x\text{Si}$ [40].

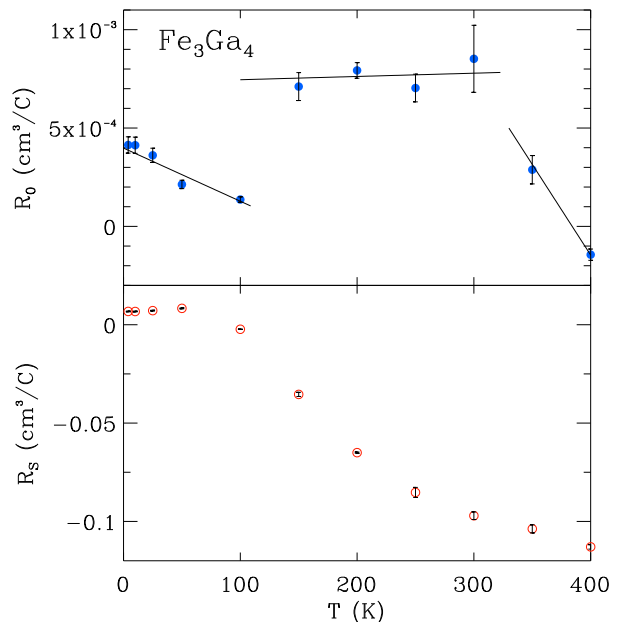


FIG. 12. Hall constants (a) The ordinary Hall coefficient,  $R_0$  of  $\text{Fe}_3\text{Ga}_4$  vs. temperature,  $T$ . Lines are guides to the eye. (b) The anomalous Hall coefficient,  $R_S$ , vs.  $T$ . Coefficients were determined from fits of the standard model of the anomalous Hall effect to the data as shown in Fig. 10.

## COMPUTATIONAL RESULTS

The experimental results presented here, as well as those obtained previously for  $\text{Fe}_3\text{Ga}_4$ , reveal a close competition between magnetic states resulting in magnetic



phase transitions easily accessible via variations in temperature or magnetic field. However, the intermediate magnetic state has proved difficult to identify and the critical temperatures and fields appear to be sensitive to disorder and sample preparation conditions. In addition, a visible jump in the electrical resistivity at  $T_2$  suggests that there may be a significant change in the electronic structure as the material enters or leaves the AFM-like phase. Thus, to gain insight into the likely magnetic ordering as well as the mechanism creating the close competition between magnetic states and the resulting sensitivities, we have performed electronic structure calculations. To gain a better understanding of the complex low symmetry monoclinic structure of  $\text{Fe}_3\text{Ga}_4$ , we display in Fig. 13 the unit cell of  $\text{Fe}_3\text{Ga}_4$  in the  $ac$ -plane labeling the planes of Fe. In this way, we demonstrate the crystal symmetries that exist along the  $c$ -axis. Further structural details are provided in the Supplementary Materials where the crystallographic data, including the site symmetries and position in fractional coordinates that result from our X-ray diffraction measurements, are presented. The four unique Fe and Ga atom sites in the unit cell along with their multiplicity and site symmetries are also shown in these tables. In Fig. 13 the system is presented as consisting of Fe planes aligned along the  $c$ -real space translation vector starting at  $C_0$  and proceeding through  $C_6$ . Several of these Fe-containing planes are related by symmetry through a mirror plane perpendicular to the  $c$ -axis and through the center of the unit cell. This makes planes  $C_1$  and  $C_6$ ,  $C_2$  and  $C_5$ , as well as  $C_3$  and  $C_4$  symmetric, leaving only the  $C_0$  plane not having a partner related to it by symmetry. In addition, in the primitive unit cell the  $C_1$  and  $C_6$  planes contain two Fe atoms while the remaining planes only contain one Fe atom. Supplementary Materials Table 4 lists the neighboring atoms for both the four symmetrically unique Fe and Ga atoms in the unit cell to demonstrate the coordination and bonding of atoms in  $\text{Fe}_3\text{Ga}_4$ . Interestingly, the Ga atoms nearest-neighbors are almost all Fe (except Ga4, which has a single Ga nearest-neighbor atom) while the Fe atoms neighbors are mainly Ga with Fe atom neighbors for the four Fe sites ranging from 17% to 43% in number.

Given the complex low symmetry structure combined with the competition between magnetic states, we carried out the electronic structure calculations using two different density functional theory based methods in order to validate our approach. We employed an all-electron full-potential linear augmented plane-wave (FLAPW) method[41] based on the WEIN2K software package[42] and a plane-wave based approach that incorporates the projected-augmented wave (PAW) method within the Vienna-*Ab-Initio* Simulation Package (VASP)[43, 44]. For both approaches the generalized gradient approximation based Perdew-Burke-Ernzerhof (PBE) exchange-correlation functionals was used[45]. The FLAPW sim-

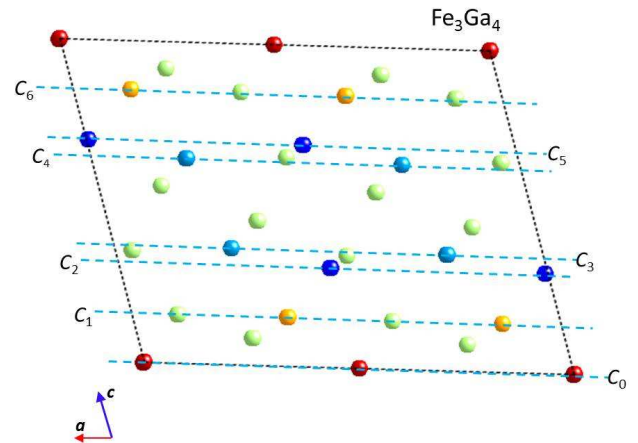


FIG. 13. Crystal structure of  $\text{Fe}_3\text{Ga}_4$  viewed along the  $b$ -axis. Atoms are identified by their color in the same way as in Fig. 1. Each plane of Fe atoms is identified by the dashed lines and labeled  $C_0$  through  $C_6$ .

ulations used the tetrahedron integration technique on a  $7 \times 8 \times 6$   $k$ -space mesh for the  $k$ -space integration, while in the VASP simulations we used the Methfessel-Paxton of order two integration method on a  $8 \times 8 \times 8$  special  $k$ -point mesh with a Gaussian smearing factor of 0.2. In both methods we carefully studied the convergence of the simulations with respect to the  $k$ -point mesh. In addition, for the VASP simulations, decreasing values of the Gaussian smearing factor were investigated. The LAPW muffin-tin sphere radii were 2.42 and 2.17 Bohr radii for Fe and Ga atoms, respectively. Careful convergence studies for the FLAPW plane-wave basis set were carried out by varying the  $RK_{max}$ , which is the product of the smallest atomic sphere radius  $R$  times the largest  $k$ -vector  $K_{max}$  where  $K_{max}$  determines the cut-off of the plane wave expansion used to represent the wavefunction in the interstitial region. A value of 9.0 was found to produce accurate total energies and forces. The VASP simulations utilized PAW potentials with the Fe atoms containing 14 valence electrons ( $3d^6 4s^1$ ) and Ga atoms with 13 valence electrons ( $3d^{10} 4s^2 p^1$ ) and a plane-wave energy cutoff equal to 293.238 eV.

The total energy in the FM and AFM states was determined in our simulations using the  $\text{Fe}_3\text{Ga}_4$  conventional cell for both the WEIN2k and VASP calculations. Both of these calculations yielded a FM state that is lower in energy by  $\sim 1$  eV / unit cell, a value much larger than the relative error (a few meV / unit cell) expected in our calculations. In addition, both approaches yielded  $\sim 0.7\%$  error in all three lattice constants as compared to the experimental values. Given the consistency between the two methods, the remainder of the presented simulation data will be from the VASP calculations.

Although, one can obtain an AFM solution for either the conventional or primitive cell, the energy difference

between the AFM and FM states is large with an equivalent temperature of 12,000 K well above the observed magnetic transitions. The large difference in energy between the FM and AFM states that the simulations find can be understood by considering the symmetry of the Fe1 crystallographic sites. Unlike a conventional cubic cell where there are no point group operators that map like atoms from one sublattice onto the other, in this conventional cell there are such point group operators. Thus, to break the symmetry and create lower energy AFM states requires careful consideration with supercells. Because the symmetry of the unit cell of  $\text{Fe}_3\text{Ga}_4$  has an inversion-type point group operation about the Fe1 site (center bottom of the structure shown in Fig. 1), the construction of supercells along the  $c$ -direction ought to lead to a lower energy AFM state. To this end, we have carried out AFM and FM simulations on  $1 \times 1 \times 2$  supercells constructed from the  $\text{Fe}_3\text{Ga}_4$  primitive unit cell. This supercell configuration produces an  $A$ -type ordering where the Fe spin moments alternate between Fe planes along the  $c$ -direction. Simulations of this arrangement produces a total Fe moment equal to zero (with individual Fe-moments ranging from 1.76 to 2.24  $\mu_B/\text{Fe}$ ) along with Ga moments that are less than 0.1  $\mu_B$  and whose sum is also zero. The simulation of the FM state yields similar sized magnetic moments yielding an average of 1.96  $\mu_B/\text{Fe}$  and ranging from 1.80 to 2.20  $\mu_B/\text{Fe}$ . These magnetic moments are somewhat larger than the average magnetic moment determined from  $M_S$  (1.5  $\mu_B/\text{Fe}$ ).

Fig. 14 displays the total energy vs.  $\beta$  for the  $1 \times 1 \times 2$  supercell in both FM and AFM states. For this AFM configuration we find that  $\Delta E_{FM-AFM} \sim -0.031$  eV/super cell at a  $\beta = 106.3^\circ$ . Although this energy difference has an equivalent temperature of 360 K, which is in good agreement with one of the experimentally observed AFM/FM transition temperatures, the simulations produce an AFM ground-state rather than the experimentally observed FM ground-state. This reversal of the ground-state from FM to AFM exists for all  $\beta$ -values used to determine the minimum energy (see Fig. 14).

Other, more complex types of AFM arrangements ( $C$ -type,  $G$ -type, etc.) can be constructed by generating larger supercells. However, if these AFM cells were to generate lower energy configurations, as compared to the  $A$ -type configuration that we used in the above calculations, an increased (more negative)  $\Delta E_{FM-AFM}$  would result enhancing the difference with experiment. Instead, we focus here on the  $A$ -type supercell exploring possible explanations for the differences between the simulations, which yield an AFM ground-state, and the experimentally observed FM low temperature state.

Experimentally the ground-state of  $\text{Fe}_3\text{Ga}_4$  is FM with antiferromagnetism accessed above 68 K in low magnetic fields. However, we observed that  $T_1$  can be somewhat lower for several crystals prior to annealing which tends to sharpen the transition and bring  $T_1$  to 68 K. Presum-

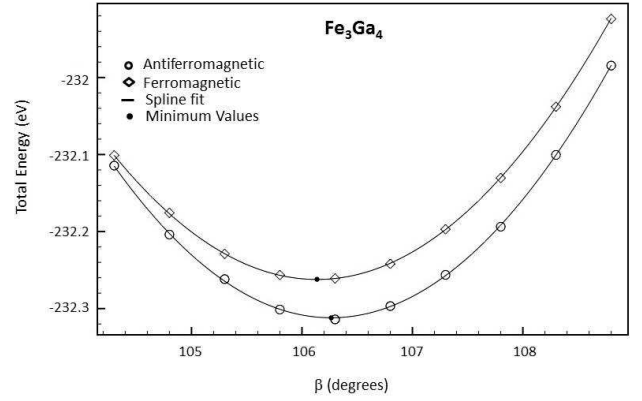


FIG. 14. Total Energy vs.  $\beta$ . The total energy change in the calculations vs. the structural angle  $\beta$  comparing the ferromagnetic (FM) and antiferromagnetic (AFM) states. We find that the AFM state is lower in energy at all  $\beta$  near the energy minimum and that the energy minima occur at very similar  $\beta$ .

ably the annealing reduces disorder and residual stress in the crystals. Thus, we have considered the effect of disorder on the magnetic ground state properties in our simulations. In  $\text{Fe}_3\text{Ga}_4$ , a simple atom counting yields only 43% Fe. The simulations described above show that a small magnetic moment on the Ga sites is primarily due to the interaction with the surrounding Fe. As Supplemental Materials Table 4 makes clear, the Ga nearest-neighbors are predominately Fe atoms. This suggests that  $\text{Fe}_3\text{Ga}_4$  has a strong ferromagnetic polarization associated with Fe despite the larger concentration of Ga in the system. The observation that the magnetic transitions are substantially affected by a relatively low temperature anneal indicates that there might be a small number of point defects in the system, most likely antisite defects where a small number of Fe atoms replace Ga. The idea is that a relatively small density of antisite defects would thereby produce small FM Fe-clusters producing a larger net polarization that potentially could lower the FM total energy below that of the AFM phase.

To explore this possibility, FM and AFM simulations have been performed on the  $1 \times 1 \times 2$  supercells where two Ga atoms have been replaced by two Fe atoms to mimic antisite defects. For this particular cell, an even number of antisites are necessary to allow for the simulation of an AFM state. Simulations were performed at the experimental  $\beta$ -value of 106.3° with the translation vectors and the atomic position fully relaxed. These simulations produce a FM ground-state that is 1.24 eV per unit cell lower in energy than the AFM state. This substantial change is not unreasonable given the rather large  $\sim 4.8\%$  concentration of Fe antisites. To reduce the antisite density to levels closer to those more likely to be present in the samples, we performed preliminary fully relaxed calculations using a  $4 \times 4 \times 4$  Monkhorst-Pack  $k$ -space integra-

tion mesh on a larger  $2 \times 2 \times 2$   $\text{Fe}_3\text{Ga}_4$  supercell where 2 Ga atoms are replaced by 2 Fe atoms corresponding to a  $\sim 1.2\%$  concentration of Fe antisites. These calculations yield a FM state that is  $\sim 0.66$  eV/supercell lower in energy than the AFM state, a significant drop in the energy difference. A simple interpolation of the energy difference between the two states based on the results of these simulations yields a rough estimate of the minimum concentration of antisite defects necessary to yield a FM ground-state of  $\sim 0.1\%$  well below the resolution of our X-ray diffraction measurements.

## DISCUSSION AND SUMMARY

We have presented an investigation of the magnetic, thermodynamic, and charge carrier properties of  $\text{Fe}_3\text{Ga}_4$  crystals to explore the sensitivity of its magnetic states to temperature and magnetic field. The measurements have not only established a moderate magnetic anisotropy in this itinerant metamagnet, but have confirmed the main features of the temperature-field magnetic phase diagram discovered in polycrystalline samples. In addition, we have identified the specific heat signal associated with the transition from the FM-to-AFM-like state near 68 K as well as the larger, more diffuse, magnetic contribution to the specific heat between room temperature and 400 K. The electrical transport is interesting because of the sharp change in  $\rho$  near  $T_2$  which is not accompanied by equally discontinuous changes in either  $\chi$  or  $C_P$ . At the same time, the transition at  $T_1$  appears to be first order showing hysteresis upon warming and cooling along with substantial changes in both  $R_0$  and  $R_S$ , yet we observe no discernible discontinuity in  $\rho$ . Furthermore, we observe a significant  $\rho_{THE}$  in the intermediate temperature range between  $T_1$  and  $T_2$  suggesting a non-coplanar magnetic state.

There are several classes of itinerant metamagnetic materials where two magnetic phases, usually ferromagnetic and antiferromagnetic, are close in energy and where temperature and magnetic fields can tip the balance in favor of a ferromagnetic or field polarized PM state. These instabilities can be accessed in a number of systems by tuning their composition via chemical substitution between end members having differing magnetic ground states. Examples include classic binary compounds,  $\text{Fe}_{1-x}\text{Rh}_x$ [46, 47], layered materials,  $\text{Hf}_{1-x}\text{Ta}_x\text{Fe}_2$ [17], and shape memory alloys,  $\text{Ni}_2\text{MnX}$  ( $X = \text{In}, \text{Sn}, \text{and Sb}$ )[23]. However, this tuning is not always necessary. Materials such as  $\text{CoMnSi}$ [19] and  $\text{Mn}_3\text{GaC}$ [48], are examples of stoichiometric compounds that have similar metamagnetic properties and temperature dependent magnetic states. The transitions between ferromagnetism and antiferromagnetism are often accompanied by either a symmetry changing structural phase transition or an abrupt change in unit cell volume. In ei-

ther case, large changes to the electronic density of states at the Fermi energy are often apparent.

For the case of  $\text{Fe}_3\text{Ga}_4$  the Hall effect data reveal changes indicative of variations in the electronic structure near  $T_1$  and  $T_2$ . The jump in  $R_0$ , as well as the sign change of the AHE, signaling a change to the reciprocal space Berry curvature, are evidence of an abrupt variation in the electronic structure in proximity to the Fermi energy. However, the very small specific heat anomaly associated with the transition at  $T_1$  is not consistent with a strong magneto-elastic coupling as would occur if the magnetic phase transition were accompanied by a change in the crystal structure. Instead, we speculate that the changes to the electronic structure at  $T_1$  and  $T_2$  are caused by entering and exiting a SDW phase. We point out that the sharp rise in  $\rho$  along with the reduction in the carrier density suggested by  $R_0$  at  $T_2$  indicate a partial Fermi surface gapping as would occur in a spin density wave state. However, we have found no obvious nesting in the complex Fermi surface that the simulations produce. In addition, the lack of a discontinuity in  $\rho(T)$  at  $T_1$  where the system reenters the FM phase with cooling, and the difference in sign of  $R_S$  below  $T_1$  and above  $T_2$ , suggests that the sections of the Fermi surface gapped in the purported SDW phase may not be completely recovered in the ground state despite the changes we observe in  $R_0$  near  $T_1$ .

Setting aside the character of the AFM phase, there remains a question as to the cause of the close competition of FM and AFM phases in this material. The complexity of the crystal structure which includes four crystallographically distinct Fe-sites each with a different magnetic moment is sure to play an important role in producing this competition. This idea is supported by our electronic structure calculations which predict that an AFM ground state is slightly favored over a FM one, but that a small density of antisite defects can stabilize the FM phase. The sensitivity to synthesis technique and annealing history of the samples that we observed would be explained as a result of the crystalline disorder tipping the balance in favor of the FM state. Thermal expansion may also play a role in driving the system toward an AFM state as pressure and Al substitution for Ga tend to stabilize the FM state to higher temperature[27]. Thus, the AFM state may very well be the preferred phase at larger lattice constants. However, because there are no indications of strong magneto-elastic coupling in the specific heat of  $\text{Fe}_3\text{Ga}_4$ , mechanisms involving a coupling of the magnetic degrees of freedom to the lattice degrees of freedom are unlikely.

We have pointed out that  $\text{Fe}_3\text{Ga}_4$  is unusual in that  $H_{mm}$  increases with  $T$  when  $H$  is parallel to the crystallographic  $c$ -axis within the AFM state[24, 25]. This behavior has also been reported in  $(\text{Hf}_{1-x}\text{Ta}_x)\text{Fe}_2$ [17] and  $\text{EuRh}_2\text{Si}_2$ [49] so that these may provide a useful point of comparison.  $(\text{Hf}_{1-x}\text{Ta}_x)\text{Fe}_2$ [21, 22] is unusual in that the

metamagnetism is thought to be associated with magnetic frustration in the AFM phase. Here there are two distinct crystallographic Fe sites, both of high symmetry. The 2a site is also a point of inversion symmetry for this lattice. As a result, the internal field is naturally canceled at the 2a site leading to paramagnetic, highly fluctuating, magnetic moments persisting at temperatures well below the Neel temperature. Thus, there is a significant magnetic entropy associated with the AFM state above that of the FM state tending to favor ferromagnetism at low  $T$ . In contrast, the  $\text{Fe}_3\text{Ga}_4$  crystal structure is not obviously layered and frustration is highly unlikely[28] so that a similar mechanism is unlikely to play a role. In  $\text{EuRh}_2\text{Si}_2$  the low- $T$  phase is thought to be a spin spiral which transitions to fan-like structure for fields along the easy plane[49]. Such a model may be possible for  $\text{Fe}_3\text{Ga}_4$  given the layered planar structure noted above. However, the nature of the anisotropy and the discontinuous changes to  $M(H)$  that we measure, see Fig. 4, make this explanation unlikely.

With the lack of crystal symmetry produced frustration, and little evidence for a magneto-elastic coupling, we are left to consider the role of the itinerant electrons and the possibility of a SDW phase along with the competing interactions caused by the four inequivalent Fe sites within the unit cell as the cause of the rich magnetic behavior we observe. It may be that  $\text{Fe}_3\text{Ga}_4$  can be considered to be intermediate between less complicated structural materials that have little competition between possible magnetic ground states, and those materials with enormous unit cells that produce spin-glass like behavior without significant disorder or obvious magnetic frustration present[50]. The drivers of such unusual behavior in  $\text{Fe}_3\text{Ga}_4$  are not obvious so that measurements of the magnetic structure are clearly needed to make progress in understanding the mechanisms for this unusual magnetic system.

## ACKNOWLEDGMENTS

Support from the NSF is acknowledged by JFD through DMR1206763, DPY through DMR1306392, and JYC through DMR1358975. Support from the DOE is acknowledged by PWA through DE-FG02-07ER46420 and JYC through DE-FG02-08ER46528. This material is based upon work supported by the National Science Foundation under the NSF EPSCoR Cooperative Agreement No. EPS-1003897 with additional support from the Louisiana Board of Regents.

---

\* ditusa@phys.lsu.edu

- [1] H. Hosono, J. Phys. Soc. Jpn., Suppl. C **77**, 1 (2008).
- [2] J. Paglione and R. L. Greene, Nature Physics **6**, 645 (2010).
- [3] G. R. Stewart, Rev. Mod. Phys. **83**, 1589 (2011).
- [4] I. Eremin, J. Knolle, R. M. Fernandes, J. Schmalian, and A. V. Chubukov, J. Phys. Soc. Jpn. **83**, 061015 (2014).
- [5] A. Pandey, B. G. Ueland, S. Yeninas, A. Kreyssig, A. Sapkota, Y. Zhao, J. S. Helton, J. W. Lynn, R. J. McQueeney, Y. Furukawa, A. I. Goldman, and D. C. Johnston, Phys. Rev. Lett. **111**, 047001 (2013).
- [6] B. Lorenz, A. M. Guloy, and P. C. W. Chu, Int. J. Mod. Phys. B **28**, 1430011 (2014).
- [7] See eg. R. J. Birgeneau, C. Stock, J. M. Tranquada, and K. Yamada J. Phys. Soc. Jpn. **75**, 111003 (2006).
- [8] R. K. Kummamuru and Y. A. Soh, Nature **452**, 859 (2008).
- [9] Y. Feng, J. Wang, D. M. Silevitch, B. Mihaila, J. W. Kim, J.-Q. Yan, R. K. Schulz, Nayoon Woo, A. Palmer, Y. Ren, J. van Wezel, P. B. Littlewood, and T. F. Rosenbaum, PNAS **110**, 3287 (2013).
- [10] H. Wagini, Z. Naturforsch. **21A**, 528 (1966).
- [11] H. Wagini, Zeit. Natur. Part A - Astrophysik Physic und Physikalische Chemie **A22** 143-144 (1967).
- [12] M. J. Philippe, B. Malaman, and B. Roques, Comptes Rendus Hebdomadaires des Seances de l' Academie des Seincies Serie C, **278**, 1093-1095 (1974).
- [13] M. J. Philippe, B. Malaman, B. Roques, A. Courtois, and J. Protas, Acta Cryst. B- Struct. Sci. **B31**, 477 - 482 (1975).
- [14] E. Strykowski and N. Giordano, Adv. Phys. **26**, 487-650 (1977).
- [15] T. Moriya and K. Usami, Solid State Commun. **23**, 935 (1977).
- [16] M. Isoda, J. Phys. Soc. Jpn. **53**, 3587 (1984).
- [17] Y. Nishihara and Y. Yamaguchi, J. Phys. Soc. Jpn. **51**, 1333 (1982).
- [18] J. B. Staunton, M. dos Santos Dias, J. Peace, Z. Gercsi, and K. G. Sandeman, Phys. Rev. B **87**, 060404(R) (2013).
- [19] A. Barcza, Z. Gercsi, H. Michor, K. Suzuki, W. Kockelmann, K. S. Knight, and K. G. Sandeman, Phys. Rev. B **87**, 064410 (2013).
- [20] K. Gschneidner, V. Pecharsky, and A. Tsokol, "Recent Developments in Magnetocaloric Materials." *Institute of Physics Publishing* (2005).
- [21] H. Wada, N. Shimamura, and M. Shiga, Phys. Rev. B **48**, 10221 (1993).
- [22] H. R. Rechenberg, L. Morellon, P. A. Algarabel, and M. R. Ibarra, Phys. Rev. B **71**, 104412 (2005).
- [23] See e.g. V. K. Sharma, M. K. Chattopadhyay, A. Khandelwal, and S. B. Roy, Phys. Rev. B **82**, 172411 (2010).
- [24] N. Kawamiya and K. Adachi, J. Phys. Soc. Jpn. **55**, 634-640 (1986).
- [25] N. Kawamiya and K. Adachi, J. Magn. Magn. Mat. **54-57**, 941-942 (1986).
- [26] H. G. M. Duijn, E. Brück, K. H. J. Buschow, F. R. de Boer, K. Prokes, and V. Sechovsky, J. Appl. Phys. **85**, 4738-4740 (1999).
- [27] H. G. M. Duijn, Ph.D. Dissertation, "Magnetotransport and magnetocaloric effects in intermetallic compounds", Van der Waals-Zeeman Institute, University of Amsterdam (2000)
- [28] M. A. Kobeissi, J. A. Hutchings, P. G. Appleyard, M. F. Thomas, and J. G. Booth, J. Phys.: Condens. Matter **11**, 6251 (1999).

- [29] H. Munekata, *Physica E* **25**, 160-170 (2004).
- [30] A. T. M. K. Jamil, H. Noguchi, K. Shiratori, T. Kondo, and H. Munekata, *J. Supercon.: Incorporating Novel Magnetism* **18**, 321-324 (2005).
- [31] N. Manyala, Y. Sidis, J. F. DiTusa, G. Aeppli, D. P. Young, and Z. Fisk, *Nature Materials* **3**, 255-262 (2004).
- [32] J. Ye, Y. B. Kim, A. J. Millis, B. I. Shraiman, P. Majumdar, and Z. Tešanović *Phys. Rev. Lett.* **83**, 3737 (1999).
- [33] N. Nagaosa, J. Sinova, S. Onoda, A. H. MacDonald, and N. P. Ong, *Rev. Mod. Phys.* **82**, 1539 (2010).
- [34] H. Gamari-Seale and S. Karavelas, *Phys. Lett. A* **23**, 31 (1966).
- [35] K. T. Moglestue, *Phys. Rev.* **178**, 781 (1969).
- [36] See e.g. Moriya, T. *Spin fluctuations in itinerant electron magnetism*, edited by Fulde, P. (Springer-Verlag, Berlin, 1985).
- [37] Y. Taguchi, Y. Oohara, H. Yoshizawa, N. Nagaosa, and Y. Tokura, *Science* **291**, 2573 (2001).
- [38] Y. Machida, S. Nakatsuji, Y. Maeno, T. Tayama, T. Sakakibara, and S. Onoda, *Phys. Rev. Lett.* **98**, 057203 (2007).
- [39] N. Kanazawa, Y. Onose, T. Arima, D. Okuyama, K. Ohoyama, S. Wakimoto, K. Kakurai, S. Ishiwata, and Y. Tokura, *Phys. Rev. Lett.* **106**, 156603 (2011).
- [40] J. F. DiTusa, S. B. Zhang, K. Yamaura, B. L. Drake, B. W. Fulfer, C. Capan, Z. Fisk, and J. Y. Chan, *to be published*.
- [41] D. J. Singh, *Planewaves, Pseudopotentials, and the LAPW Method, 2nd Ed.* (Springer-Verlag, Berlin, 2006).
- [42] P. Blaha, K. Schwarz, G. Madsen, D. Kvasnicka, and J. Luitz, *WIEN2K, An Augmented Plane Wave+Local Orbitals Program for Calculating Crystal Structure* (K. Schwarz Technical University, Wien, Austria, 2001).
- [43] G. Kresse and J. Furthmüller, *Phys. Rev. B* **54**, 11169 (1996).
- [44] G. Kresse and D. Joubert, *Phys. Rev. B* **59**, 1758 (1999).
- [45] J. P. Perdew, K. Burke, and M. Ernzerhof, *Phys. Rev. Lett.* **77**, 3865-3868 (1996).
- [46] M. Fallot, *Ann. Phys. (Paris)* **10**, 291 (1938).
- [47] G. Shirane, C. W. Chen, P. A. Flinn, and R. Nathans, *Phys. Rev.* **131** (1963).
- [48] J.-P. Bouchaud, R. Fruchart, R. Pauthenet, M. Guillot, H. Bartholin, and F. Chaisse, *J. Appl. Phys.* **37**, 971 (1966).
- [49] S. Seiro and C. Geibel, *J. Phys.: Condens. Matter* **26**, 046002 (2014).
- [50] D. C. Schmitt, J. C. Prestigiacomo, P. W. Adams, D. P. Young, S. Stadler, and J. Y. Chan, *Appl. Phys. Lett.* **103**, 082403 (2013).



# Supplemental Materials for Competing magnetic states, disorder, and the magnetic character of $\text{Fe}_3\text{Ga}_4$

J. H. Mendez,<sup>1</sup> C. E. Ekuma,<sup>1,2</sup> Y. Wu,<sup>1</sup> B. Fulfer,<sup>3</sup> J. C. Prestigiacomo,<sup>1</sup>  
W. A. Shelton,<sup>2,4</sup> M. Jarrell,<sup>1,2</sup> J. Moreno,<sup>1,2</sup> D. P. Young,<sup>1</sup> P. W.  
Adams,<sup>1</sup> A. Karki,<sup>1</sup> R. Jin,<sup>1</sup> Julia Y. Chan,<sup>5</sup> and J. F. DiTusa<sup>1,\*</sup>

<sup>1</sup>*Department of Physics & Astronomy,*

*Louisiana State University, Baton Rouge, LA 70803, USA*

<sup>2</sup>*Center for Computation and Technology,*

*Louisiana State University, Baton Rouge, LA 70803, USA*

<sup>3</sup>*Department of Chemistry, Louisiana State University, Baton Rouge, LA 70803, USA*

<sup>4</sup>*Department of Chemical Engineering,*

*Louisiana State University, Baton Rouge, LA 70803, USA*

<sup>5</sup>*Department of Chemistry, University of Texas at Dallas, Richardson, TX 75080, USA*

(Dated: April 23, 2015)

We include supplementary crystallographic information on  $\text{Fe}_3\text{Ga}_4$  to support the measurements and electronic structure calculations presented in the main text of the paper.

## CRYSTALLOGRAPHIC TABLES

Crystallographic tables for the structure of  $\text{Fe}_3\text{Ga}_4$ .

Formula	<b><math>\text{Fe}_3\text{Ga}_4</math></b>
Space Group	$C2/m$
$a$ (Å)	10.0979(15)
$b$ (Å)	7.6670(15)
$c$ (Å)	7.8733(10)
$\alpha$	90.00
$\beta$	106.298(10)
$\gamma$	90.00
$V$ (Å <sup>3</sup> )	585.06 (16)
$Z$	6
Crystal size (mm)	0.03 x 0.06 x 0.08
Temperature (K)	294
Density (g cm <sup>-3</sup> )	7.602
$\theta$ Range (°)	2.70 - 32.51
$\mu$ (mm <sup>-1</sup> )	37.811

TABLE I: Crystal data

---

\* ditusa@phys.lsu.edu

Collected reflections	7303
Unique reflections	1121
$R_{int}$	0.066
$h$	$15 \leq h \leq 15$
$k$	$-11 \leq k \leq 11$
$l$	$-11 \leq l \leq 11$
$\Delta\rho_{max}$ (e $\text{\AA}^{-3}$ )	1.812
$\Delta\rho_{min}$ (e $\text{\AA}^{-3}$ )	-1.365
GoF	1.081
Extinction coefficient	0.00172(9)
$^a R_1(F)$ for $F_o^2 > 2\sigma(F_o^2)$	0.0281
$^b R_w(F_o^2)$	0.0501

TABLE II: Data Collection and Refinement. Note that  $^a R_1 = \sum ||F_o| - |F_c|| / \sum |F_o|$  and  $^b wR_2 = [\sum w(F_o^2 - F_c^2)^2 / \sum w(F_o^2)^2]^{1/2}$ ;  $w = 1/[\sigma^2(F_o^2) + (0.0191P)^2 + 1.0814P]$  at 294 K for  $\text{Fe}_3\text{Ga}_4$ .

No.	Site	Wyckoff	Site	x	y	z	Occ.	$U_{eq}(\text{\AA}^2)$
	Notation		Symmetry					
1	Fe1	2c	2/m	0	0	0	1.00	0.0049(2)
2	Fe2	4i	m	0.49442(7)	0	0.31088(10)	1.00	0.00557(16)
3	Fe3	4i	m	0.22488(7)	0	0.63791(9)	1.00	0.00511(16)
4	Fe4	8j	1	0.13563(5)	0.20024(7)	-0.15176(7)	1.00	0.00542(12)
5	Ga1	4i	m	0.26998(6)	0	0.08446(8)	1.00	0.00849(14)
6	Ga2	4i	m	0.04142(6)	0	0.34817(8)	1.00	0.00825(14)
7	Ga3	8j	1	0.60841(4)	0.20297(6)	0.15127(5)	1.00	0.00794(11)
8	Ga4	8j	1	0.35194(4)	0.18674(6)	0.44958(6)	1.00	0.00889(11)

TABLE III: Experimental crystallographic data for  $\text{Fe}_3\text{Ga}_4$ .

Site	Fe	Ga
<b>Fe1</b>	2.565(6) [ $\times 4$ ]	2.619(7) [ $\times 2$ ], 2.654(4) [ $\times 2$ ], 2.659(5) [ $\times 4$ ]
<b>Fe2</b>	2.749(4) [ $\times 1$ ], 2.766(6) [ $\times 2$ ], 2.9484(16) [ $\times 1$ ]	2.459(16) [ $\times 1$ ], 2.477(6) [ $\times 1$ ], 2.488(6) [ $\times 2$ ], 2.520(8) [ $\times 2$ ]
<b>Fe3</b>	2.598(6) [ $\times 2$ ], 2.749(4) [ $\times 1$ ]	2.503(16) [ $\times 1$ ], 2.538(11) [ $\times 2$ ], 2.558(2) [ $\times 2$ ], 2.639(7) [ $\times 4$ ], 2.7219(15) [ $\times 1$ ]
<b>Fe4</b>	2.565(6) [ $\times 1$ ], 2.598(6) [ $\times 1$ ] 2.766(6) [ $\times 1$ ], 2.921(18) [ $\times 1$ ]	2.488(2) [ $\times 1$ ], 2.498(10) [ $\times 1$ ], 2.528(11) [ $\times 1$ ], 2.5358(14) [ $\times 1$ ], 2.5737(10) [ $\times 1$ ], 2.5746(10) [ $\times 1$ ]
<b>Ga1</b>	2.459(16) [ $\times 1$ ], 2.488(2) [ $\times 2$ ], 2.498(10) [ $\times 2$ ], 2.619(7) [ $\times 2$ ]	2.9336(7) [ $\times 2$ ], 2.9417(7) [ $\times 2$ ]
<b>Ga2</b>	2.503(16) [ $\times 1$ ], 2.528(11) [ $\times 1$ ], 2.654(4) [ $\times 2$ ], 2.7219(15) [ $\times 1$ ]	2.7456(12) [ $\times 1$ ], 2.9157(7) [ $\times 2$ ]
<b>Ga3</b>	2.477(6) [ $\times 2$ ], 2.538(11) [ $\times 2$ ], 2.5737(10) [ $\times 1$ ], 2.5746(10) [ $\times 1$ ], 2.586(3) [ $\times 1$ ], 2.659(5) [ $\times 1$ ]	
<b>Ga4</b>	2.488(6) [ $\times 2$ ], 2.524(11) [ $\times 2$ ], 2.5358(14) [ $\times 1$ ], 2.558(2) [ $\times 2$ ], 2.639(7) [ $\times 2$ ]	

TABLE IV: Fe and Ga neighbor distances. Multiplicities are given in square brackets.